Reactive and Functional Polymers 217 (2025) 106494

Contents lists available at ScienceDirect

Reactive and Functional Polymers

journal homepage: www.elsevier.com/locate/react

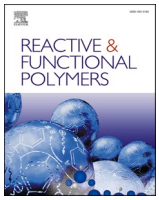

Development of a high-performance dual-curing Vitrimeric acrylate/epoxy system for 3D printing: Analysis of thermal effect and network evolution

A. Escribá-Flores [a], Szymon Gaca [b,c], X. Fernández-Francos [d], Sandra Schlögl [b,c], A. Fabregat-Sanjuan [a,*]

[a] Department of Mechanical Engineering, Universitat Rovira i Virgili, Av. Països Catalans 26, 43007 Tarragona, Spain
[b] Polymer Competence Center Leoben GmbH, Sauraugasse 1, 8700 Leoben, Austria
[c] Chair of Chemistry of Polymeric Materials, Montanuniversitaet Leoben, Otto Glöckel-Straße 2/IV, 8700 Leoben, Austria
[d] Thermodynamics Laboratory, ETSEIB, Universitat Politècnica de Catalunya, Av. Diagonal 647, 08028 Barcelona, Spain

ARTICLE INFO

Keywords:
Vitrimer
Dual curing
Additive manufacturing
High tensile strength
Relaxation
Recycling

ABSTRACT

Vat photopolymerization (VPP) 3D printing has gained significant attention for its ability to fabricate complex geometries with high resolution and excellent surface finish using relatively low-cost equipment. However, developing materials that combine mechanical robustness, geometric fidelity, and recyclability remains challenging. Here, we present a dual-curing vitrimeric acrylate/epoxy system that transitions from a highly deformable up to 80 % of strain in the intermediate state (ultimate tensile strength of 0.7 MPa) to a mechanically robust final state (ultimate tensile strength of 66 MPa) after thermal treatment. The system also supports effective repair via bonding protocols, recovering substantial mechanical integrity, thanks to the transesterification bond exchange. In spite of some shortcomings related to the irreversible changes in network structure upon thermal cycling, these results demonstrate a promising versatile platform for sustainable, durable, and repairable VPP components.

1. Introduction

3D printing with vat photopolymerization (VPP) has gained significant interest in recent years due to its ability to produce parts with high precision, excellent surface finish, and complex geometries [1–4]. These features make it especially attractive to industries such as automotive, aerospace, education, research, medicine, dentistry, and jewelry, for both customized prototype manufacturing and fabrication of functional components. In recent years, this technology has evolved into various variants such as DLP [5], SLA [6], LCD [7], and CLIP [8], and has also led to advanced techniques such as micro-SLA [9] and two-photon absorption polymerization [10], aimed at manufacturing microstructures. However, despite these advancements, significant limitations still exist in the performance of the materials currently used. Acrylate- and methacrylate-based systems stand out for their high reactivity and rapid photopolymerization but generate heterogeneous polymer networks that result in brittle materials with modest mechanical strengths. In addition, they exhibit high volumetric shrinkage during polymerization, which can compromise the dimensional stability of the parts and induce internal stresses that lead to defects such as cracks or warping, affecting interlayer adhesion [11]. On the other hand, epoxy resins, while offering excellent mechanical properties and low shrinkage, require cationic photoinitiators and slower reactions than radical-based systems, which reduces their appeal in terms of processability [12]. Furthermore, their higher viscosity may make them more challenging to print compared to lower viscosity acrylic formulation [13]. Beyond processability limitations, traditional thermosets cannot be easily recycled or repaired, posing a barrier to the growing demands for sustainability.

In this context, the development of dynamic covalent polymer networks, such as vitrimers, opens new opportunities to overcome these challenges. Vitrimers allow for the combination of dimensional stability and mechanical properties of thermosets with unique capabilities for reprocessing, repair, and recycling [14,15]. Several recent studies have demonstrated their potential for applications in demanding thermal, chemical, and mechanical environments. These dynamic networks, activated thermally above the glass transition temperature (Tg) and the onset temperature for bond exchange reactions, exhibit a flow associated with the exchange of bonds within the network [16,17]. Stress

* Corresponding author.
E-mail addresses: armandoalfredo.escriba@urv.cat (A. Escribá-Flores), szymon.gaca@pccl.at (S. Gaca), xavier.fernandez@upc.edu (X. Fernández-Francos), sandra.schloegl@pccl.at, sandra.schloegl@unileoben.ac.at (S. Schlögl), a.fabregat@urv.cat (A. Fabregat-Sanjuan).

https://doi.org/10.1016/j.reactfunctpolym.2025.106494
Received 15 July 2025; Received in revised form 11 September 2025; Accepted 23 September 2025
Available online 24 September 2025

relaxation dynamics of vitrimers are strongly influenced by network structural effects (crosslinking density, Tg) in addition to the intrinsic reaction kinetics of the bond exchange process [18–21]. It can be generally stated that vitrimer networks with lower Tg show evidence of the possibility to undergo relaxation and repair processes at moderate to high temperatures [22], thereby minimizing exposure to potential thermal degradation. In contrast, networks with higher Tg and crosslinking densities typically require higher temperatures and longer times [18] to relax or repair, which may increase the risk of compromising the thermal integrity of the network. In these cases, thermal degradation could degrade the dynamic groups responsible for reconfiguration, limiting the effectiveness of reprocessing. The development and implementation of vitrimer systems adapted to VPP 3D printing technologies represents a promising pathway to achieving advanced materials that meet technical requirements while offering recycling, repair, and reprocessing capabilities.

A number of 3D-printable vitrimeric systems have been reported in the literature, showing excellent resolution, low volumetric expansion coefficients, intermediate viscosities, and in some cases, high mechanical properties [14,23–25]. However, 3D-printed materials with high glass transition temperatures (Tg) may require prolonged thermal treatments at elevated temperatures in order to promote the bond exchange reactions and complete relaxation of the materials. Such elevated temperatures, typically in the range of 150–200 °C [18,26], can lead to thermal degradation, or else irreversible network rearrangement and loss of volatile components as a consequence of bond exchange processes, therefore compromising the ability of the material to be further reprocessed [27]. However, these adverse thermal effects and their implications for the structural and functional stability of vitrimer systems with high Tg have not been widely reported or systematically studied in the literature, which represents a relevant limitation for their precise characterization and practical application in demanding conditions.

This work presents and characterizes a dual system with vitrimer capabilities, based on acrylic and epoxy-acid reactions, designed for processing by 3D printing via vat photopolymerization (VPP). Such combination exploits the excellent reactivity and processability of acrylic monomers with the low volumetric shrinkage and outstanding mechanical properties of the epoxy resin. The mechanical performance of the material in bulk state was investigated by means of tension, direct shear and torsion tests, relevant for the structural design of solid components. The repair capabilities of these materials were studied and evaluated by means of adhesive tensile tests. The effect of prolonged exposure to high temperatures on the polymer network was investigated in order to elucidate the changes in the composition and structure of the polymer networks.

2. Materials and experimental part

2.1. Materials

Glycerol 1,3-diglycerolate diacrylate (GLYDA, 348.35 g/mol), ethyleneglycol phenyl ether methacrylate (FEMA, 206.24 g/mol) used such as reactive diluent, 2-hydroxyethyl methacrylate (HEMA, 130.14 g/mol), glutaric anhydride (GLU, 114.10 g/mol) to produce a bonding agent between both networks, bis(2,4,6-trimethylbenzoyl)-phenylphosphine oxide (BAPO) and zinc acetylacetonate $Zn(acac)_2$ were purchased from Sigma-Aldrich. Diglycidyl ether of bisphenol A (DGEBA, 187 g/eq.) was purchased from PO.INT.ER S.r.l. All products were used without further purification except DGEBA, which was dried for 2 h under vacuum at 80 °C prior to use. The different reagents are shown in Scheme 1 (a).

2.2. Preparation of coupling agent GLUHEMA

Preparation of coupling agent GLUHEMA (244.24 g/mol) was carried out by stoichiometric esterification of hydroxyl groups of HEMA with anhydride groups of GLU, leading to a carboxyl-methacrylate derivative, as seen in Scheme 1 (b). The reaction was carried out in bulk at 80 °C for 6 h in magnetic stirring, as reported previously [28].

2.3. Preparation of formulations

The formulations used in this work are summarized in Table 1. FEMA was kept at a constant content of 20 wt%, while the amount of GLYDA was varied between 1 and 5 wt%. The remaining of the formulation up to 100 wt% consisted of GLUHEMA and DGEBA with a stoichiometric ratio between carboxyl groups of GLUHEMA and epoxy groups of DGEBA. Radical photoinitiator BAPO and epoxy-acid and transesterification catalyst $Zn(acac)_2$ were added with fixed proportions of 2 phr and 5 phr, respectively. The formulations were prepared by first mixing the acrylic components GLYDA, FEMA and GLUHEMA, followed by the introduction of BAPO and the catalyst for the epoxy-acid reaction

Table 1
Composition of the formulations expressed as total weight ratios of the different components. BAPO and Zn(acac)2 amounted to 2 and 5 phr, respectively.

Reagents	GLUHEMA1_20 (wt %)	GLUHEMA2_20 (wt %)	GLUHEMA5_20 (wt %)
GLYDA	1.00	2.00	5.00
GLUHEMA	44.74	44.17	42.47
FEMA	20.00	20.00	20.00
DGEBA	34.26	33.83	32.53

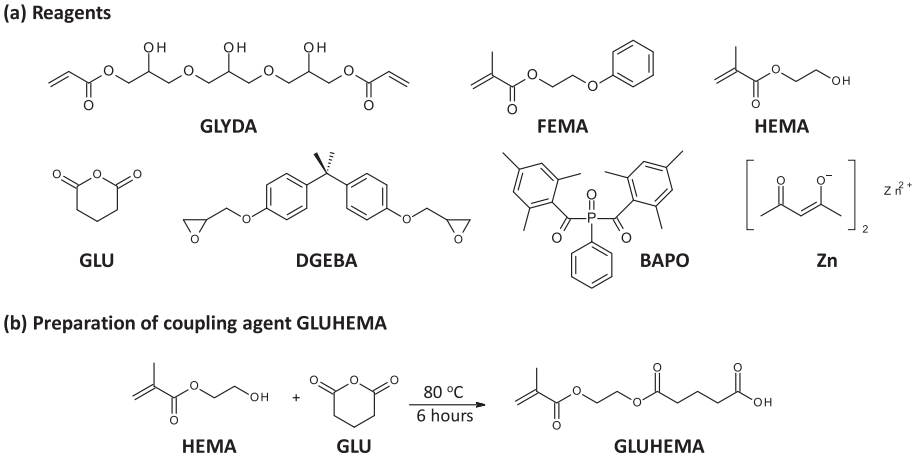

Scheme 1. (a) Reagents used in this work (b) Reaction for the formation of the coupling agent GLUHEMA.

and transesterification $Zn(acac)_2$ and vigorous magnetic stirring for 10 min. DGEBA was finally added and the mixture was homogenized again with magnetic stirring, aiming at obtaining formulations with low viscosity and high reactivity both in the intermediate state after printing and thermal treatment.

2.4. Preparation of materials

For the printing process, an ASIGA MAX-UV 3D printer (Sydney, Australia) equipped with a UV light source at 385 nm and an ELEGOO Mars 4 DLP (China, Shanghái) with light source of 405 was used. The samples were printed with a power of 4.77 mW/cm^2, a resolution of 0.07 mm in the Z direction and an exposure of 6 s for each layer.

The Jacobs working curve of the different formulations was determined in order to optimize the printing conditions:

$$C_d = D_p Ln\left(\frac{E}{E_c}\right) \quad (1)$$

Where Cd (μm) refers to the curing depth or thickness of the sample, Ec represents the critical energy, and E (mJ·cm^{-2}) denotes the maximum energy of the radiation reaching the surface. Dp (μm) corresponds to the light's penetration depth. The plot of Cd against ln(E) should produce a straight line with intercept ln(Ec) and slope Dp. Three samples of each formulation were irradiated at 4.77 mW/cm^2 using a 385 nm wavelength (provided by the ASIGA-MAX-UV 3D printer), with exposure times varying between 10 and 60 s on a circular area of 10 mm in diameter. The curing depth (Cd) was measured using a micrometer, and E was determined from the light intensity and exposure time.

The printed pieces were then removed from the printer and washed with isopropanol to remove any excess material. Afterward, the samples were placed in a DentalFarm UV curing oven (photopol VAC + GAS) under UV light. This UV curing process lasted for 10 min at a pressure of −0.09 MPa and an intensity of 200 W, ensuring the completion of the acrylic reaction within the system. This state is defined as the intermediate state.

The intermediate materials were subjected to thermal treatment at 100 °C for one hour, followed by 180 °C for one more hour, in order to activate and complete the epoxy-acid reaction. After the thermal treatment the system is defined as final state or fully cured material.

2.5. Thermal and physicochemical characterization

A differential scanning calorimeter (DSC) Mettler DSC 821e calorimeter, equipped with a Hamamatsu Lightning Cure LC5 (medium-pressure Hg—Xe lamp) and two lightguides, one directed at the sample and the other at the reference, was used to monitor the photopolymerization of acrylic groups upon exposure to UV light, corresponding to the 1st reaction stage. Around 5 mg of the solution was placed in open aluminum pans under a nitrogen atmosphere. The samples were first stabilized at 30 °C for 2 min before irradiation. They were exposed to light for 12 min at 30 °C with an intensity of 20 mW/cm^2 and then kept in the dark for an additional 2 min. A second scan was performed and used as a baseline to correct the thermal effect of the UV light, in order to determine the heat of reaction. All experiments were carried out with a nitrogen flow of 50 mL/min.

A DSC Mettler DSC 3+ equipped with an intra-cooler was used to determine the kinetics of the 2nd reaction stage corresponding to the epoxy-acid reaction. Samples ranging from 0.010 to 0.025 g of the intermediate material were analyzed at a constant heating rate of 10 °C/min from −50 °C to 250 °C. All experiments were carried out with a nitrogen flow of 50 mL/min. To evaluate the curing kinetics under isothermal conditions, the second reaction stage was analyzed by subjecting the samples to an isothermal treatment at 180 °C for 3 h.

Mettler DSC 3+ was also used to analyze the evolution of the Tg of fully cured samples upon prolonged thermal treatment at 180 °C. The samples were subjected to repeated cycles of isothermal treatment for 1 h followed by a dynamic scan at 10 °C/min to determine changes in the Tg.

A Mettler Toledo TGA/DSC 1 was used to analyze the thermal stability of fully cured samples. Around 10 mg of each sample was placed in alumina crucibles with pierced lids and heated at 10 °C/min from 25 °C to 700 °C in a nitrogen atmosphere. Isothermal tests were conducted at 180 °C for 24 h. All experiments were carried out with a nitrogen flow of 50 mL/min.

Infrared spectroscopy was carried out using a Bruker Vertex 70 FTIR spectrometer equipped with an attenuated total reflection (ATR) accessory (GoldenGate™ by Specac Ltd.), collecting spectra in the mid-infrared region across a spectral range from 4000 cm^{-1} to 600 cm^{-1}, with 20 scans averaged for each spectrum. Samples of the uncured liquid, intermediate and fully cured materials were analyzed.

To analyze the volatile compounds released during the thermal treatment, an EGY/PY-3030D Multi Shot Pyrolizer (Frontier Laboratories, Japan) coupled to a gas chromatograph and a mass spectrometer GCMS-QP2010 Ultra (Shimadzu, Japan) was used. Solid samples of approximately 6 mg were placed in stainless steel crucibles with a volume of 80 μL (Eco-Cup, Frontier lab, Fukushima, Japón). The samples were first heated to 70 °C and held isothermally for 5 min. Subsequently, the temperature increased at a constant rate of 10 K/min up to 180 °C, where it was maintained for 4 h. The column used was an EGA tube (deactivated metal capillary, L = 2.5 m, inner diameter = 0.15 mm), which conducted the volatile decomposition products directly to the detector (quadrupole mass filter) using helium as carrier gas. In the mass spectrometer, the decomposition products were ionized with an energy of 70 eV and scanned within the range of 40–400 *m/z*.

The viscosity of the solutions was measured using a TA Instruments Discovery HR-20 rheometer, equipped with parallel aluminum plates of 25 mm diameter. The tests were conducted in shear rate sweep, applying a shear rate range from 1 s^{-1} to 1000 s^{-1} to evaluate the rheological behavior of the samples at 30 °C. The gap between the plates was kept at 100 μm.

2.6. Shrinkage-stress measurements

The shrinkage and shrinkage stress analysis were performed using an MCR 501 rheometer (Anton Paar, Austria) coupled with an Omnicure S2000 UV lamp without additional light filters, operating at a power density of 35 mW/cm^2. The experiments were conducted for gap values of 0.05 and 0.10 mm in thickness, with a 25 mm diameter parallel plate and a transparent glass base. These experiments were carried out with this configuration, considering average setup values for DLP 3D printing. The shrinkage analysis was carried out by setting the normal force to 0 N and measuring the evolution of the gap. In order to determine the stress, the gap was fixed and the evolution of the normal force was monitored.

Shrinkage analysis of printed parts in their final state after thermal treatment was also conducted. Cylindrical models with a diameter of 8 mm and a height of 10 mm were printed and cured according to the thermal protocol described previously. Dimensional measurements were performed using a Moore & Wright 201-01DAB Digital Micrometer 0–25 mm / 0–1″ (Sheffield, United Kingdom), and the values were compared with the original CAD model to evaluate dimensional deviations.

2.7. Thermo-mechanical and mechanical characterization

Thermomechanical analysis was conducted using a DMA Q800 (TA Instruments). Rectangular samples with dimensions of 10 × 50 × 2 mm were prepared for the experiment. The measurements were performed in tensile mode with an oscillation strain of 0.1 %. The samples were initially equilibrated at −20 °C for 10 min, followed by a controlled temperature ramp at 3 °C/min up to 200 °C. The glass transition

temperatures (Tg) of the materials were determined by identifying the peak of the tan δ curve corresponding to the α-relaxation.

Stress relaxation tests were performed using a DMA Q800 in tensile mode under 1 % strain with a preload of 0.003 N at 180 °C for a duration of 1400 min. To investigate changes in vitrimeric behavior, samples with varying curing times were analyzed under these conditions.

Tensile tests were performed in accordance with ISO 527-1/2 standards, utilizing a loading rate of 1.5 mm/min and a 500 N load cell with the Shimadzu AGS-X series 10 kN tabletop model (Shimadzu Scientific Instruments). Deformation was measured using a TRViewX video extensometer (Shimadzu Scientific Instruments), and the entire system was controlled through Trapezium X Testing Software (Shimadzu Scientific Instruments).

Direct-shear strength was measured using a shear test method and tooling developed in [29] (see Fig. S-1) utilizing a loading rate of 1.5 mm/min and a 500 N load cell with the Shimadzu AGS-X series 10 kN tabletop model (Shimadzu Scientific Instruments). This tooling was designed to effectively counteract bending forces appearing in lap-shear testing, providing a more precise evaluation of adhesive performance where the base material and the adhesive material have similar mechanical properties. The tooling features a constant 0.01 mm gap in the shear zone, maintained throughout the test due to the geometry of the tooling and the symmetry of the forces generated. Joint samples were prepared as described in the following section.

For the torque analysis, an Instron E3000 machine was used in combination with specimen that was fabricated at half the standard dimensions, following the guidelines provided in ISO 18338. 0.2 rev/min was the velocity used until reaching the failure, as no specific standard exists for characterizing printed parts. Instead, a lower loading rate was employed to ensure a more accurate evaluation of the material's behavior.

2.8. Joining treatments

The joint analysis process involves evaluating the bonding performance under various treatment scenarios, following the protocols developed in [29,30]. Fig. S-2 illustrates the treatments applied to both the intermediate and final states of the formulations, enabling a detailed assessment of their effects. Fig. S-2 (a) depicts the two treatments applied to the intermediate state of the formulation. The first treatment, JTF, involves applying adhesive to the interface immediately after printing the parts, using the same bulk material solution to evaluate bonding. The parts are then subjected to light treatment for 10 min under vacuum. Finally, the samples are tested for tensile strength. The second treatment, JTFF, begins with an initial light treatment after printing, followed by the application of adhesive to the interface and a second light treatment for 10 min. The samples are subsequently tested for tensile strength.

Fig. S-2 (b) focuses on the final state of the formulations, showing two treatments used to analyze bonding. The first treatment, JTC, builds on the JTF process by adding a thermal treatment after the 10-min light exposure under vacuum. The samples are heated in an oven for 1 h at 100 °C, followed by another hour at 180 °C. The second treatment, JTCC, starts with a light treatment on freshly printed parts, followed by thermal treatments at 100 °C and 180 °C for 1 h each. Adhesive is then applied to the interface, and the samples undergo a second light treatment, followed by additional heating at 100 °C and 180 °C for 1 h each. After the thermal treatments, the bonded samples are subjected to tensile tests to evaluate their mechanical performance. Additionally, shear tests on bonded joints were conducted following the defined procedures for the JTC treatment, referred to as JSC.

2.9. Recycling

The recycling process involved pulverizing the material in its final state using a mill (A 11 basic Analytical mill), subjected to five cycles of one minute each. The milled material was then placed in a metal mold, shaped to match the dimensions of tensile test specimens (ISO 527-2, 5B), and compacted under 10 MPa using two heated plates at 180 for 6 h. The resulting specimens were subsequently evaluated through tensile tests and thermomechanical analyses.

3. Results and discussion

3.1. Kinetics of dual-curing process

Herein, the intermediate state is defined by the first stage of the dual-curing process. In particular, the exposure to UV light initiates the radical by chain-growth polymerization of the (meth)acrylates, as seen in Scheme 2 (a), leading to the formation of a lightly crosslinked network structure. A random copolymer structure is formed containing crosslinking sites resulting from GLYDA, and side chains from FEMA and GLUHEMA, which are acting as chain extenders, as seen in Scheme 2 (b).

The final state is defined by the 2nd curing stage, in which heating leads to the activation of the epoxy-acid reaction, catalyzed by Zn $(acac)_2$, as seen in Scheme 3 (a). The side carboxyl groups from GLUHEMA in the acrylic network react with the epoxy groups from DGEBA, leading to coupling of acrylic chains in the network and therefore further crosslinking, as illustrated in Scheme 3 (b). Consequently, a dense crosslinked network structure is obtained at the end. However, it is worth noting that all the crosslinking sites from GLYDA and reacted GLUHEMA bear dynamic β-hydroxyester groups in their structure, which should allow complete relaxation of the stress by thermo-activated transesterification [28].

The 1st reaction stage of the dual-curing process was investigated by means of photoDSC. Fig. 1 (a) provides the thermograms of the different formulations, showing clearly the activation of the chain-growth polymerization of (meth)acrylic groups upon activation of the photoinitiator by exposure to UV light, as seen in Scheme 2 (a). No relevant changes in reaction rate with composition were observed. The DSC scan at 10 °C/min of partially cured materials in Fig. 1 (b) shows the curing exotherm corresponding to the epoxy-acid reaction catalyzed by Zn(acac) $_2$ [31], evidencing that the kinetics of the 2nd curing stage are hardly affected by the change in composition either. Therefore, the change in the content in GLYDA is not expected to affect the global processing of these materials in the 3D-printing process nor the subsequent thermal curing in the oven. On the other hand, an isothermal DSC analysis at 180 °C was performed to monitor the exothermic reaction between epoxy and acid

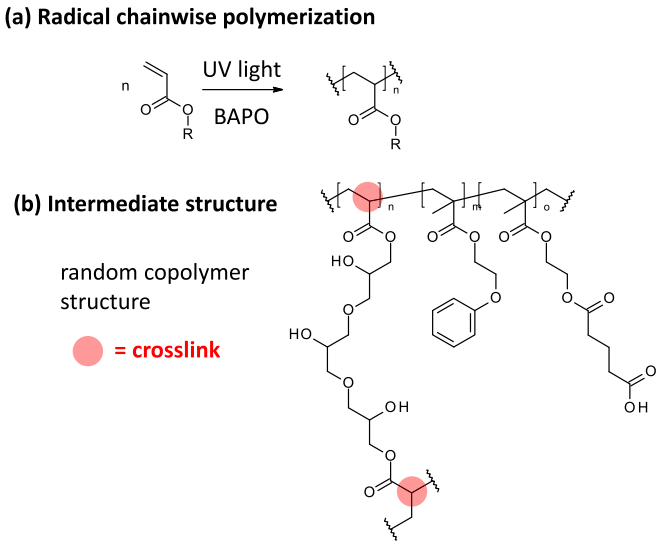

Scheme 2. (a) Light-induced radical chain-growth polymerization of (meth) acrylates and (b) resulting intermediate random copolymer structure.

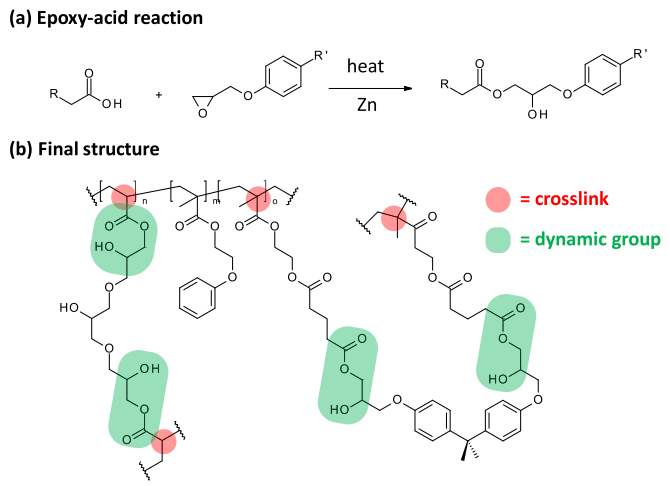

Scheme 3. (a) Thermally induced epoxy-acid reaction and (b) final network structure.

groups catalyzed by $Zn(acac)_2$, corresponding to the GLUHEMA1_20 formulation (see Fig. S-3). The results show that the reaction proceeds rapidly, with conversion degrees exceeding 97 % after 30 min. This is highly desirable, as it enables high conversion levels to be achieved in relatively short times, which is advantageous from a processing standpoint.

The FTIR analysis of the initial, intermediate, and final materials further demonstrated effective control over the curing process. Fig. S-4 displays the infrared spectrum of the GLUHEMA1_20 formulation. A comparison between the uncured liquid and the partially cured sample clearly shows the complete reaction of the (meth)acrylate groups, indicated by the disappearance of absorption peaks at 1300–1340 cm^{-1}, and 1610–1640 cm^{-1}. Additionally, the presence of epoxy groups is highlighted by absorption bands between 915 and 925 cm^{-1}, which are not affected by the UV-curing process and disappear almost completely in the fully cured material, therefore confirming the orthogonality of the dual-curing process and the effective control of the curing sequence.

3.2. Thermal and thermomechanical characterization

DMA analysis was conducted for the different formulations in their fully cured state. Fig. S-5 (a) shows the peaks in the loss factor (tan δ) corresponding to the α-relaxation of the material, related to the glass transition of the network. It can be seen that the relaxation starts around 40–50 °C, with a Tg around 70–80 °C, taken as the tan δ peak temperature. The storage modulus and loss modulus values presented in Fig. S-5 (b) and (c), respectively, demonstrate a similar behavior for all formulations, showing only minor differences. There is a certain trend of increasing Tg and reducing intensity of tan δ peak with increasing GLYDA content, that can be related to the shorter length of GLYDA bridges connecting acrylic networks, in comparison with the length of the longer GLUHEMA+DGEBA+GLUHEMA structures formed in the 2nd reaction stage (see Scheme 3 (b)), reducing the mobility of the network structure. However, the resulting crosslinking density, determined from the relaxed storage modulus E', is similar in all cases, as seen in Fig. S-5 A single peak is observed in all cases, evidencing the homogeneity of the final network structure, resulting from the coupling of (meth)acrylic chains after the epoxy-acid reaction between the DGEBA and the acid groups in the side chains of GLUHEMA, taking place in the 2nd reaction stage. The evolution of the loss modulus E" shows similar trends as the loss factor. A comparison with the recycled samples at 180 °C for 6 h and 10 MPa is shown in Fig. S-5.

The thermal stability of the materials was studied with TGA under non-isothermal (dynamic) and isothermal conditions. Thermogravimetric analysis at 10 K/min in Fig. S-6 (a) shows a single, well-defined degradation stage in all formulations, indicating a homogeneous degradation process. However, degradation starts at slightly lower temperatures in materials with lower GLYDA content. Specifically, $T_{2\%}$ is approximately 270 °C for GLUHEMA1_20 and GLUHEMA2_20, increasing to 300 °C for GLUHEMA5_20. Similarly, $T_{5\%}$ rises from around 310 °C in GLUHEMA1_20 and GLUHEMA2_20 to 335 °C in GLUHEMA5_20. These results reflect enhanced thermal stability with higher GLYDA content. These subtle shifts in degradation temperatures may be associated with a higher crosslink density in the (meth)acrylate phase, which restricts polymer segment mobility and delays thermal decomposition. Nonetheless, assessing the thermal behavior under reprocessing conditions is more relevant, as potential changes in network structure or loss of volatile components could affect material reuse. For that purpose, isothermal degradation experiments were conducted at 180 °C. Fig. S-6 (b) shows that the weight loss during 24 h exposure at 180 °C is around 2 % in all cases, with minor differences between the different materials. This slight loss in volatiles indicates that minimal changes in the network structure are expected, although the impact on the reprocessing capabilities of the materials will have to be analyzed in any case [27]. Table 2 shows the principal thermal and thermomechanical properties of the formulations.

3.3. Analysis of processing parameters

The printability of the formulations is influenced by both the reactivity during layer formation and their viscosity. The Jacobs curve defines the minimum energy required for layer formation, serving as a comparative parameter for resins and providing insight into the ease with which layers can be formed. Regarding viscosity, formulations with

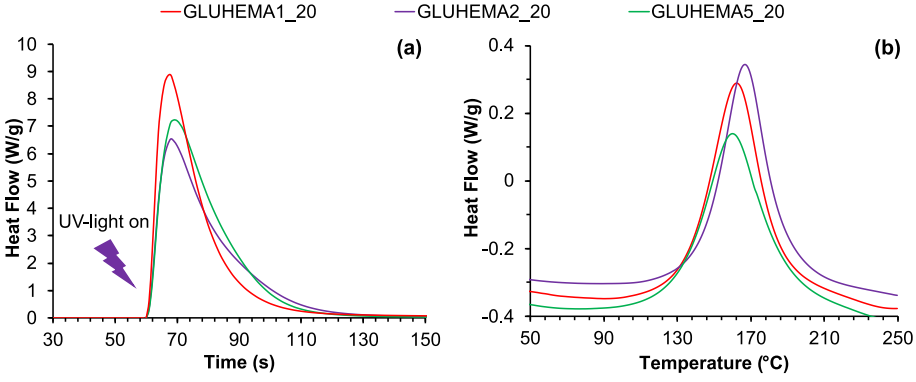

Fig. 1. Photo-DSC thermogram at 30 °C showing the reaction kinetics of the 1st stage UV-activated free-radical polymerization of methacrylates present in the formulation (a). DSC thermogram at 10 °C/min depicting the reaction kinetics of the 2nd stage thermally activated epoxy-acid reaction (b). A similar trend is observed across all formulations when comparing their behavior in the intermediate state after light irradiation and in the final state after thermal treatment.

Table 2
Thermal and thermomechanical properties of the formulations.

Formulation	Tg intermediate state* (°C)	Tg Final state (°C)**	E glassy (Mpa)	E rubbery (Mpa)	Crosslink density final state (mol/m^3)	T2% (°C)
GLUHEMA1_20	−12.68	72	2026	12.55	1250.05	270
GLUHEMA2_20	−7.75	79	1922	12.74	1267.78	300
GLUHEMA5_20	−7.65	82	2014	12.85	1252.62	335

* Value corresponds to the phase transition measured by DSC in the intermediate state.
** Value corresponds to the peak observed in DMA.

high viscosity require longer processing times and more complex setups, while those with low viscosity allow smoother material flow, efficiently filling the gaps between the formulation, vat, and platform.

Fig. 2 (a) shows the Jacobs working curves for the formulations, all displaying similar behavior and confirming excellent photoreactivity. The dashed blue line marks the exposure dose used during printing, which was carefully chosen to ensure sufficient curing and reliable interlayer adhesion, while preserving lateral resolution. This setup proved effective for producing mechanically stable parts without printing defects.

Fig. 2 (b) shows the viscosity profiles of the formulations across a range of shear rates. All formulations exhibit non-Newtonian, shear-thinning behavior characteristic of pseudoplastic fluids, which may be attributed to the alignment of their components under shear. Notably, the viscosities remain relatively low throughout the tested range, decreasing from approximately 500 mPa·s at low shear rates (0.1 s^{-1}) to below 100 mPa·s at high shear rates (1000 s^{-1}). These values are much lower than the critical value of self-leveling (3000 mPa·s) [32], indicating excellent flow properties. Within this shear rate window, the formulations exhibit excellent printability, facilitating smooth processing during 3D printing. Fig. 3 presents both photographs and microscope images of a complex printed element, highlighting the excellent deformability of the material in its intermediate state (Fig. 3 (a) and (b)), as well as the outstanding surface finish (Fig. 3 (c)) and high lateral resolution (XY plane) achieved during printing(Fig. 3 (d)).

The photo-rheology analysis allowed for the investigation of both shrinkage and mechanical behavior of the solutions during photocuring. The selected setup closely simulates conditions typically encountered in VPP 3D printing. Shrinkage induced by the photoreaction was determined, with an average reduction of 5.79 ± 0.96 %, as shown in Fig. 4 (a). This relatively small value of shrinkage can be attributed to the reduced (meth)acrylic fraction in the formulation, due to the volume fraction of epoxy monomer that is not participating in the 1st reaction stage, and to the large equivalent weight of the acrylic components, specially the monofunctional GLUHEMA coupling agent, in comparison with conventional polyfunctional or smaller (meth)acrylates, Table S-1 compares the lineal shrinkage values of various vitrimeric systems suitable for processing via VPP. Moreover, to evaluate the effect of thermal treatment on shrinkage, it was observed that heating had a positive impact on the geometrical stability of the printed parts, showing a linear volumetric increase relative to the initial gap, with a value of 1.22 ± 0.96 %.The thermal expansion induced during the post-curing process at 180 °C caused a slight network dilatation, which, upon cooling, resulted in minimal final shrinkage. This behavior can be attributed to a volumetric compensation provided by the epoxy reaction occurring in the later stages, leading to coupling of (meth)acrylate chains and the formation of a denser and more dimensionally stable network, with higher Tg, ultimately yielding parts with only minor geometrical deviations. Epoxy reactions are known to produce less curing shrinkage than acrylic reactions. It is hypothesized that this lower curing shrinkage of the 2nd stage reaction, in combination with the higher Tg of the material, leading to lower volumetric shrinkage upon cooling, may contribute to this observed effect.

Fig. 4 (a) shows that the onset of the shrinkage formation takes place shortly after irradiation starts. Indeed, the evolution of storage and loss moduli, G' and G" respectively, in Fig. S-7 (b), reveals the transition from a liquid solution to a solid in less than 20 s, stabilizing after 30 s of irradiation, which indicates the completion of the (meth)acrylate reactions. It can be observed that gelation and network formation, determined from the crossover of G' and G"(this occurs around second 64, about 4 s after irradiation, as is shown in the scaled chart in Fig. S-7), coincides with the onset of the appearance of curing shrinkage measured by the instrument. The final value of the modulus G' evidences the formation of a lightly crosslinked network structure.

Additional tests were carried out with different compositions and gaps (see Fig. S-8) The comparison of the formulations GLUHEMA1_20, GLUHEMA5_20, and GLUHEMA40_20 evaluated with a 100 µm gap shows a clear trend across the formulations, with GLUHEMA1_20 exhibiting the lowest final shrinkage. This sequence is consistent and in line with expectations, given that increasing GLYDA content should lead to lower gel point conversion and therefore higher curing shrinkage after gelation. When GLUHEMA1_20 is tested at a 400 µm gap (dotted line), the shrinkage curve is smoother and overall, more attenuated, which is attributed to reduced light penetration in the thicker layer, leading to slower polymerization kinetics and delayed apparent gel point. These observations suggest that better printing accuracy may be

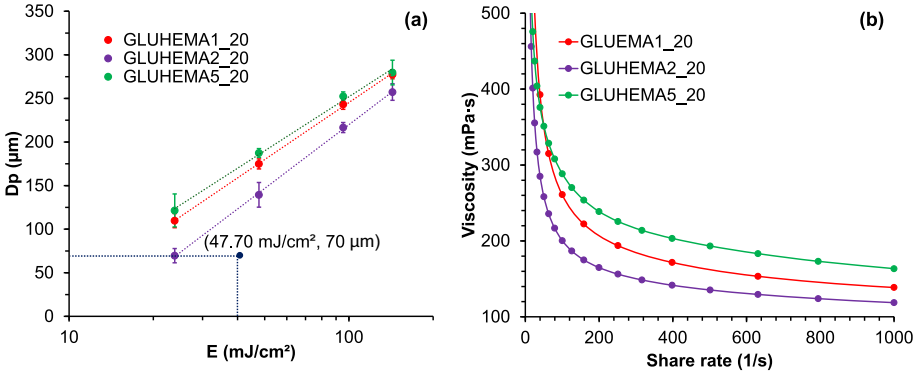

Fig. 2. Jacobs working curves for all evaluated formulations are presented. The purple dot indicates the dose used for printing elements, while a layer thickness of 70 µm was maintained (a). The viscosity of different formulations at various shear rates is shown (b). (For interpretation of the references to colour in this figure legend, the reader is referred to the web version of this article.)

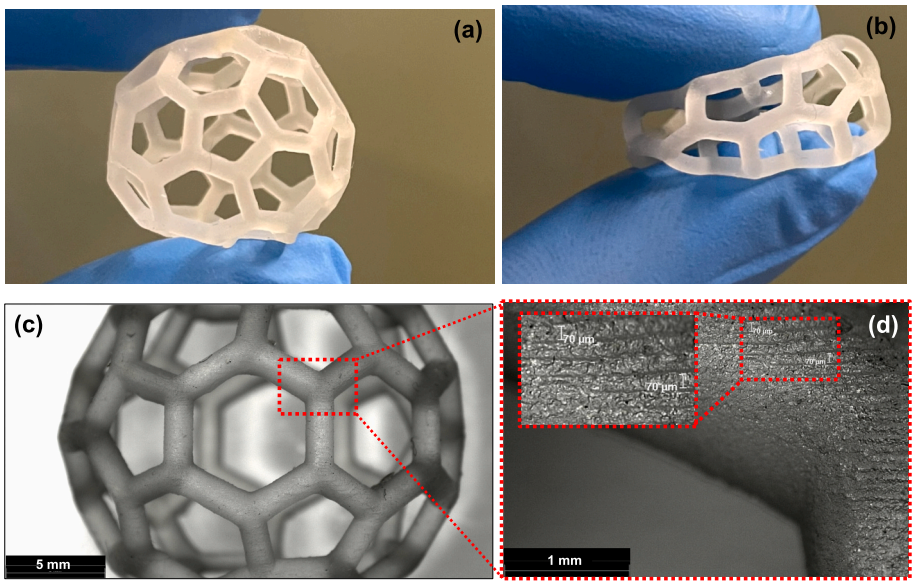

Fig. 3. Part printed with the GLUHEMA1_20 formulation, demonstrating the capability of these systems to fabricate complex structures (a); deformation capacity of the system in its intermediate state (b); microscopy image showing an excellent surface finish (c). In the magnified view of a node of the structure (d), the layer thickness matches the value described in the Methods section, with no significant surface defects observed.

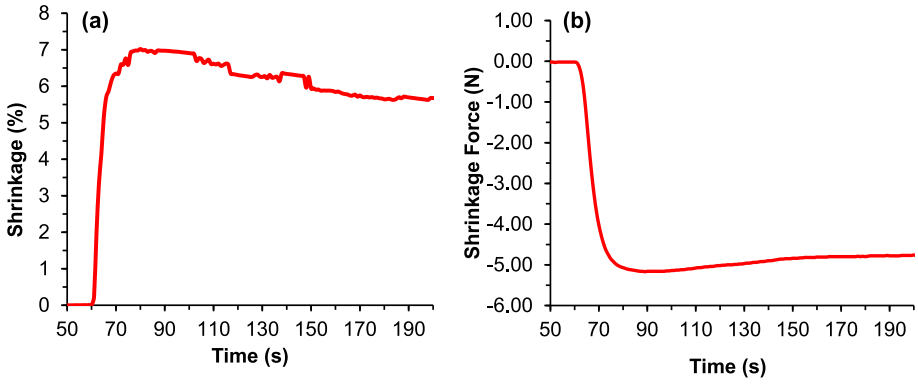

Fig. 4. GLUHEMA1_20 evolution of shrinkage (a); GLUHEMA1_20 for the evolution of the shrinkage force (b).

achieved with dual-curing formulations containing reduced GLYDA content, due to lower shrinkage-induced stress, although this may result in a somewhat longer printing time in order to ensure a sufficient degree of conversion after gelation has been reached.

On the other hand, when the gap was fixed, it was possible to observe the level of stress experienced by the layers during their formation. Fig. 4 (b) illustrates how the GLUHEMA1_20 formulation, with a fixed gap of 0.1 mm, experiences stress due to shrinkage during the photocuring process. It is evident that the system reaches a maximum force of −5.14 N, which is relatively low. Taking into consideration the plate diameter of 25 mm, this corresponds to a stress of approximately 0.010 MPa, which is about 10 % of the maximum tensile stress the material can withstand in its intermediate state, as will be seen later in the analysis of the mechanical properties of the materials. Therefore, the stress generated during photocuring should not compromise the structural integrity of the printed layers. Fig. S-9 shows a comparison of force levels for the same 0.10 mm gap in two commercial systems and various configurations of components present in the GLUHEMA system. This figure demonstrates that, on one hand, the stress levels during photocuring are lower compared to those found in commercial systems. Moreover, there is a systematic effect of delaying and decreasing shrinkage stress with decreasing GLYDA content. Both effects are explained by the increase in gel point conversion caused by the reducing content in GLYDA crosslinker, therefore increasing gel time and reducing shrinkage-induced stress after gelation. This can be beneficial in terms of printing accuracy due to the lower geometrical distortion produced by the shrinkage stress, but this is accomplished with an increasing UV exposure, eventually resulting in a somewhat higher printing time. These results are in agreement with the shrinkage measurements shown in Fig. S-8.

In order to highlight the changes taking place in the network structure throughout the dual-curing process, the 2nd reaction stage was also monitored in the photorheometer. Fig. 5 shows the temperature profile (a) and the evolution of the storage modulus G' in both curing stages (b). Initially, the system is stabilized at 30 °C to ensure isothermal conditions. It is then exposed to UV radiation for 7 min (around 420 s), after which the lamp is turned off and the thermal curing stage begins. In this phase, the sample is gradually heated until reaching 180 °C, a temperature that is maintained for nearly 1 h. In the first stage, a rapid and sustained increase in the storage modulus is observed, attributed to the formation of the (meth)acrylate network initiated by the photopolymerization of (meth)acrylates, with G' around 0.18 MPa, as described before. Subsequently, as the temperature increases, the thermal curing stage is activated, leading to further crosslinking of the network structure. This is evidenced by an increase in G' that is initially slow but then accelerates substantially after 10 min at 180 °C, reaching

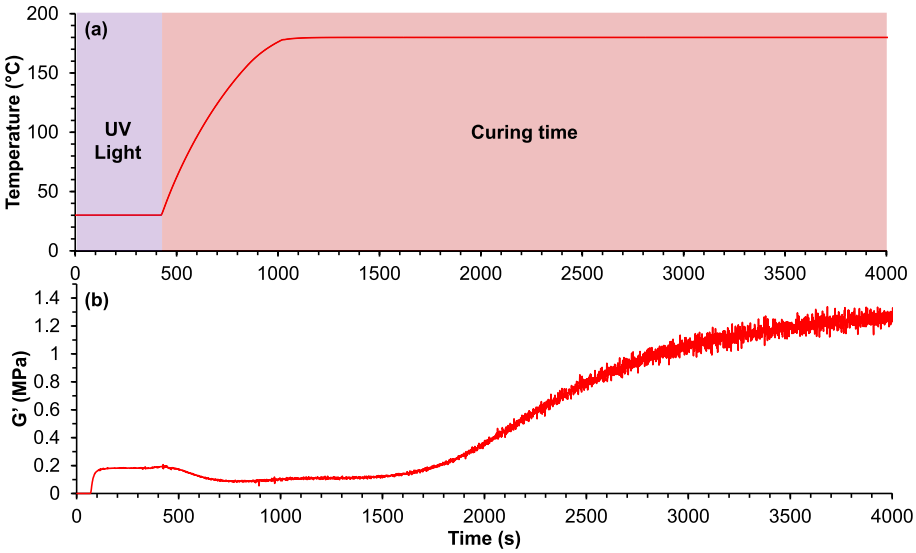

Fig. 5. Thermal and UV radiation profile (a), and evolution of G' throughout all treatments during network formation of GLUHEMA1_20 formulation (b).

values of G' around 1.2 MPa, which represents nearly a 10-fold increase compared to the intermediate material before the heating process. This slower progression, compared to the behavior in Fig. S-7, is evident in Fig. 5 (b). The differences observed between both techniques are mainly due to the measurement conditions imposed by each instrument. DSC provides precise thermal control and operates with small sample masses, enabling rapid thermal homogenization and an accurate representation of curing kinetics under isothermal conditions. In contrast, the rheometer evaluates the system's evolution under mechanical stimuli, using larger volumes where thermal transfer may be less efficient. These methodological differences explain the discrepancies observed: while DSC can reach degrees of conversion above 97 % in less than 15 min at 180 °C, under more heterogeneous rheological conditions, at least 30 min may be required to achieve a comparable degree of cure.

The initially slow growth in G' in the thermal curing stage indicates that there is an extended stability of the intermediate material in terms of structure and thermal-mechanical properties. Even though the epoxy-acid reaction may already have taken place, it may be necessary to have a significant conversion of epoxy and acid groups in order to produce a substantial increase in crosslinking density. This may be rationalized taking into consideration that the epoxy-acid reaction is a random stepwise reaction, and that a new crosslink may be formed only when both epoxy groups of a diepoxy monomer have reacted (see Scheme 3). This means that for a conversion of epoxy groups equal to $x = 0.2$, the fraction of new crosslinks formed will be equal to $x^2 = 0.04$; for $x = 0.5$, the fraction of new crosslinks will be to $x^2 = 0.25$. It is therefore quite clear that only when the conversion of epoxy groups is close to 1, the crosslinking process is complete. An additional benefit is the precise control of network formation in the thermal curing stage. Rapid curing processes can induce network defects or internal stresses that compromise mechanical integrity, while excessively slow curing is impractical for industrial applications and can lead to incomplete crosslinking [33,34]. Therefore, balancing the curing rate is essential to maintain both the dimensional stability and stiffness of the final material, ensuring its performance and reliability. Moreover, the simultaneous occurrence of bond exchange reactions between formed β-hydroxyester bonds (see Scheme 3) may also help alleviate the formation of possible defects caused by reaction-induced shrinkage stress. In this experiment, the rheometer showed a volumetric expansion of 2.47 %, which was close to the measurements obtained using the micrometer after thermal treatment in printed cylinders. The measurement was taken after the rheometer had cooled down. The relatively high volumetric expansion value may be attributed to the fact that, during the experiment, all components in contact with the sample inside the rheometer were heated and experienced thermal expansion together with the printed part.

3.4. Mechanical characterization

3.4.1. Tensile test

The mechanical properties of the intermediate and fully cured materials were analyzed in detail. Fig. 6 (a) shows the stress-strain curves corresponding to the tensile analysis of intermediate materials. It can be clearly observed that the intermediate materials have a clearly ductile behavior, with elastic modulus ranging from 1 to 2.5 MPa, depending on the formulation, and strain that exceeds 50 % (see Table 3). The values of elastic modulus are of a similar magnitude as the values of shear storage modulus G' determined from the photorheological analysis of the 1st reaction stage (see Fig. S-7). The mechanical behavior is primarily determined by the composition of the (meth)acrylic network formed in the 1st reaction stage, higher GLYDA content leading to higher modulus, and the presence of unreacted epoxy monomer acting as plasticizer.

In contrast, in the fully cured state, the material exhibits a rigid behavior with significantly improved mechanical properties, as shown in Fig. 6 (b). The formulations display similar behavior, with consistent values of elastic modulus between 2.5 and 3.5 GPa, maximum strain between 3 and 4 %, and ultimate stress between 50 and 70 MPa (see Table 3), depending on the formulations. These elevated values of modulus and ultimate stress and reduced strain at break are explained by the fact that the materials are in the glassy state at room temperature, along with extensive hydrogen bonding between hydroxyl groups formed in the epoxy-acid reaction and numerous ester groups present in the network structure providing them with a very strong cohesive energy density and efficient chain packing [35], hence explaining the high modulus values.

These mechanical properties clearly outperform many of those reported for commercial acrylic formulations in the literature. Fig. 7 (a) presents a comparison of ultimate tensile strength of other dynamic polymer systems capable of being processed via 3D printing [36–46]. Fig. 7 (b) presents a comparison between tensile strength and Young's modulus, highlighting a noticeable gap in the stiffness typically achieved by dynamic polymer networks. The material developed in this work stands out by exhibiting significantly higher rigidity at room temperature, which can be attributed to the high epoxy content and the strong interactions between the components of the formulation.

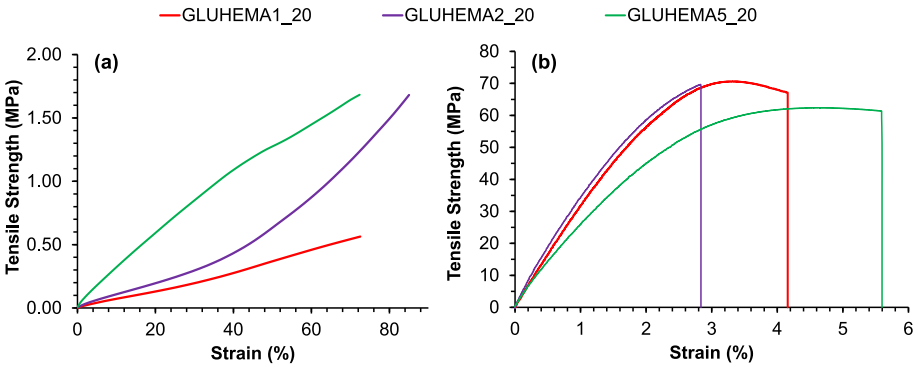

Fig. 6. Comparison of mechanical properties for different formulations in the intermediate state (a) and in the final state (b).

Table 3
Primary mechanical properties of each formulation, measured in the intermediate and final states.

Formulation	*E*-Intermediate state (Mpa)	σ max-Intermediate state (MPa)	E-Final state (GPa)	σ max-Final state (MPa)	Toughness-Final state (MJ/m^3)
GLUHEMA1_20	0.97 ± 0.06	0.57 ± 0.04	2.5 ± 0.4	66.09 ± 5.16	2.06 ± 0.45
GLUHEMA2_20	1.61 ± 0.13	0.68 ± 0.05	3.3 ± 0.5	66.47 ± 5.5	2.16 ± 0.55
GLUHEMA5_20	2.33 ± 0.27	1.61 ± 0.16	3.5 ± 0.4	65.2 ± 6.08	2.31 ± 0.38

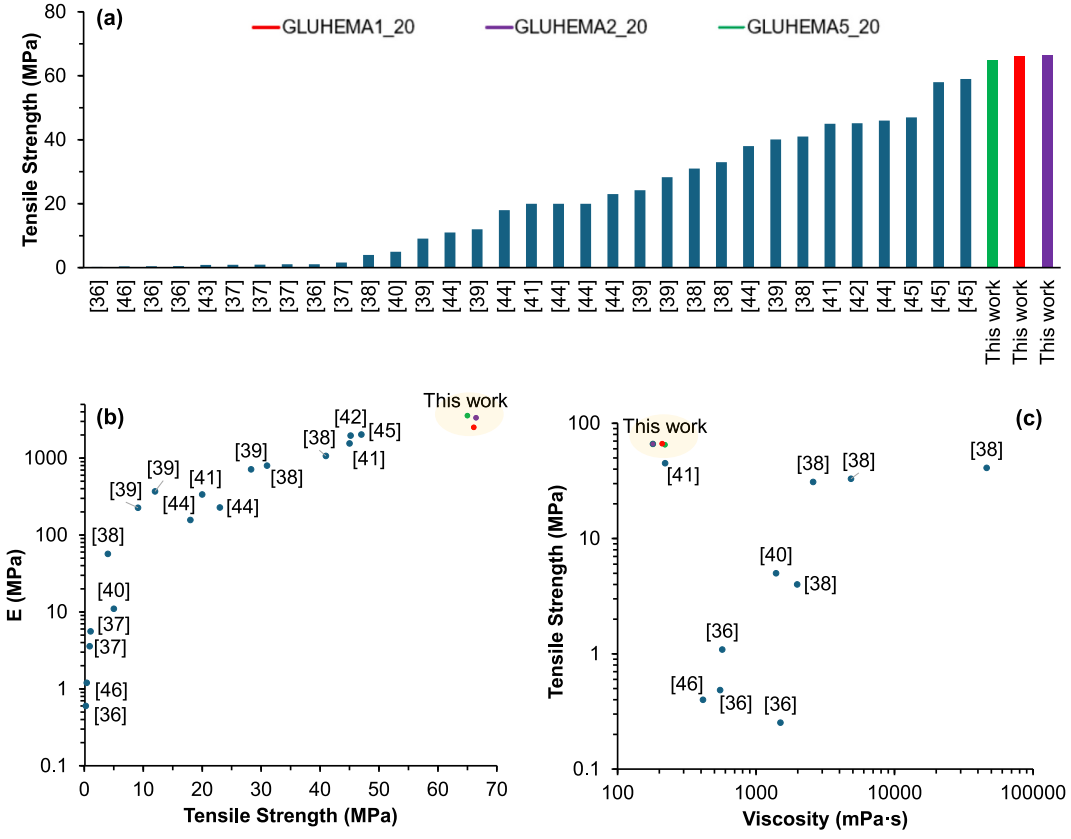

Fig. 7. A comparison is made between 3D-printable dynamic polymer systems and their tensile strength (a). Additionally, tensile strength and Young's modulus values reported in the literature are compared (b), along with an analysis of the relationship between maximum tensile strength and the viscosity of the systems (c).

Moreover, the careful balance between the reactive diluent (meth)acrylates and the crosslinking agents contributes to both enhanced mechanical properties and excellent processability. Additionally, Fig. 7 (c) shows that tensile strength and viscosity are frequently reported together in the literature, as both parameters are critical for ensuring printability and mechanical performance. As illustrated, our formulations successfully bridge the typical gap between low viscosity and high tensile strength, offering a balanced profile suitable for advanced 3D printing applications.

In order to analyze the benefits of the dual-curing processing, we evaluated the mechanical performance of joints created following different procedures, in intermediate and fully cured materials. The analysis of the joints included four different treatments to assess the mechanical behavior and performance of the system in each case. Fig. 8

(a) compares mechanical properties of intermediate joined samples of GLUHEMA1_20 formulations, prepared following the different methodologies described in the experimental section. It can be observed that the properties of the JTF and JTFF are comparable to those of the bulk material, indicating excellent adhesion. The slight improvement observed in the intermediate state with the JTF treatment is due to the interaction of residual groups in the network with the groups at the interface, enhancing adhesion and performance. In contrast, the JTFF treatment shows a slight decrease in its properties. However, the elastic modulus and strain remain nearly identical to those of the bulk material.

On the other hand, the performance of the joints subjected to thermal treatments (JTC and JTCC) compared to the fully cured bulk material is shown in Fig. 8 (b), which displays stress-strain curves for each treatment and for the bulk material of the GLUHEMA1_20 formulation. The curves are observed to be quite similar to each other. Furthermore, the values of elastic modulus and strain at break also exhibit minimal differences among them. This clearly indicates that the applied thermal treatment (JTC and JTCC) has only minor variations in terms of maximum tensile strength, elastic modulus, and strain at break. Such a comparison highlights the excellent adhesive tensile properties of this system, which is an attribute rarely explored in 3D-printed materials but extremely important in structural design.

3.4.2. Torsion and direct shear test

With the purpose of providing a more complete mechanical characterization of the materials, particular emphasis is placed on the analysis of shear behavior, a critical factor in structural design, but often overlooked in the characterization of systems employed in VAT photopolymerization-based 3D printing. Shear stress (τ), shear modulus (G), and angular deformation (γ) were studied using different techniques.

Fig. 9 (a) presents the results obtained from a torsion test conducted on the GLUHEMA1_20 formulation in its fully cured state, where a maximum shear strength of 52.82 ± 2.23 MPa, a shear modulus of 872.31 ± 30.86 MPa, and an angular deformation of 0.73 ± 0.20 were observed. The experimental shear modulus was compared with the theoretical value calculated using the following Eq. 2:

$$G = \frac{E}{2(1+\nu)} \tag{2}$$

where G is the shear modulus, E is the Young's modulus, and ν is the Poisson's ratio. This equation assumes that the material is homogeneous and isotropic, which allows its elastic behavior to be described using the constitutive equations of linear elasticity. Under these conditions, the deformations in the elastic region are functions of the applied stresses and are uniformly distributed in all directions. For the theoretical calculation of the shear modulus with eq. 2, a value of 2508.24 MPa was used for E and 0.35 for v, based on data obtained from the tensile test using a video extensometer, yielding a value of 928.88 MPa that is very similar to the experimental value from the torsion test. This agreement validates the assumptions of linearity, elastic behavior, and material isotropy, allowing engineers to confidently use simpler tensile test data (E and ν) to estimate shear properties without the need for additional, more complex torsion tests. This is particularly useful in early-stage material selection, finite element modeling, and structural simulations, where complete mechanical characterization is often unavailable.

Additionally, Fig. 9 (b) compares the maximum shear strength of all formulations in their final state, obtained using the tooling described in the Methods section and also used in [29]. The results obtained with the tooling show a good correlation with those of GLUHEMA1_20 determined from the torsion test, with no significant differences between the formulations. Furthermore, Fig. 9 (b) also shows the maximum shear strength of a joint (following the procedure JTC in a shear specimens) made with the GLUHEMA1_20 formulation in its final state. Although the obtained values are slightly lower than in the bulk state, the variations fall within the expected margins, confirming the consistency of the material's properties under joint conditions.

3.5. Stress relaxation behavior

The presence of dynamic β-hydroxyester groups in all the bridging crosslink sites between the (meth)acrylic chains, either originally present (GLYDA) or formed in the 2nd reaction stage between GLUHEMA and DGEBA, should enable complete relaxation of the stress in these materials and therefore enable interesting reprocessing capabilities, as recently described [28]. Because of this, we analyzed the relaxation behavior of the different materials, the results being shown in Figs. 10 (a). All systems exhibit a slow relaxation process, with approximately 63 % of the initial stress being relaxed within 10 to 15 min. After 200 min, full relaxation is achieved. Notably, the three formulations display very similar relaxation profiles, as seen in the corresponding graph. Fig. 10 (b) presents the relaxation curve for the GLUHEMA1_20 formulation after extended thermal treatment at 180 °C, revealing an increase in relaxation times after longer curing times. This phenomenon can be explained by a reorganization of the polymer chains within the existing network architecture, that may be explained by the occurrence of transesterification reaction of β-hydroxyester groups, and other possible transesterification events. This may result in a more densely crosslinked network structure, leading to slower stress relaxation, as reported previously [47]. However, there is also the risk of formation of volatile components and irreversible network rearrangement, eventually resulting in a loss in reprocessing capabilities of the material [48]. Indeed, Fig. 10 (b) seems to suggest that successive relaxation cycles result in incomplete relaxation of the stress due to the irreversible formation of permanent bonds in the network structure.

Such evolution could be related to the weight loss experienced by the materials under isothermal treatment at 180 °C, as shown in Fig. S-6 (b). A moderate weight loss is observed that could be with the formation of volatile components because of the bond exchange reactions taking

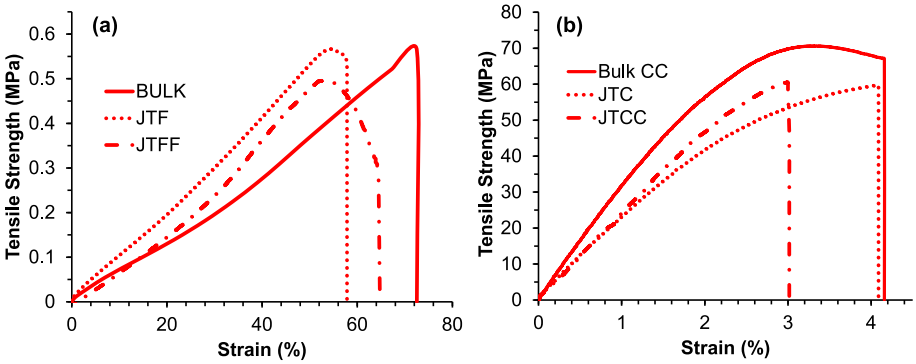

Fig. 8. Comparison of mechanical properties for different bonding protocols in the intermediate state (a) and in the final state (b).

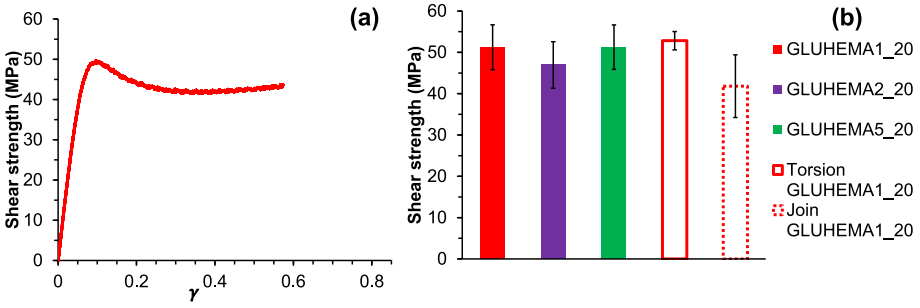

Fig. 9. $\tau - \gamma$ of 3D printed samples for the formulation GLUHEMA1_20 in the final state, determined from torsion tests (a). Shear strength for all the formulations obtained by using the tooling and torsion test (b).

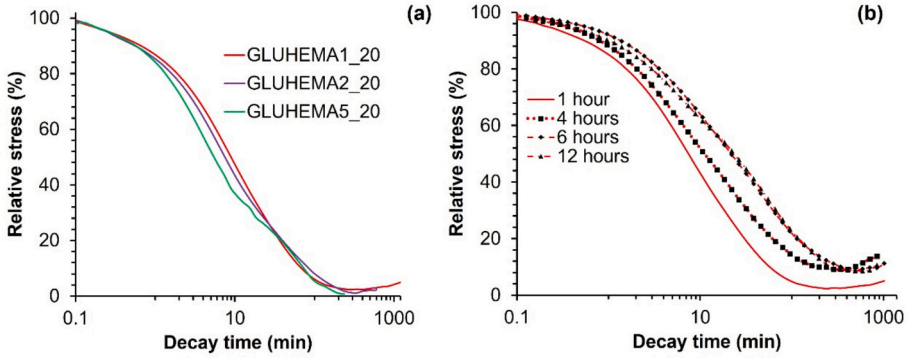

Fig. 10. Relaxation profiles at 180 °C for all formulations in their fully cured state (a). Relaxation profiles for the formulation GLUHEMA1_20 with curing times of 1, 4, 6, and 12 associated hours (b).

place and eventually leading to irreversible changes in the network structure. Indeed, the evolution of Tg over extended thermal treatment at 180 °C was analyzed with DSC. The results in Fig. S-11 reveal a progressive increase in Tg, eventually stabilizing after 8–10 h, which can be related to the weight loss observed (Fig. S-6 (b)) and the reduction in stress relaxation capabilities of the materials (Fig. 10 (b)). The progressive increase in the Tg observed via DSC suggests that the primary polymer chains are not being degraded, as their breakdown would typically lead to a decrease in Tg due to the loss of structural integrity. The analyses of the reprocessed samples presented in Figs. S-5 and S-10 further confirm that thermal treatment negatively affects the final properties of the materials. The mechanical pulverization prior to thermal exposure not only leads to the rupture of permanent bonds within the polymer network but also significantly increases the surface area of the samples. This enlarged surface area may enhance the release of volatile components during thermal treatment, thereby contributing to the observed lower performance.

Such undesired side effect represents a serious setback for the effective exploitation of the reprocessing capabilities of 3D-printed components following this strategy. In order to gain more understanding on this degradation process and their negative effects, we analyzed the materials by GC–MS. Preliminary results shown in Supporting Information (Fig. S-12 and Fig. S-13) evidence the presence of fragments compatible with small aromatic components that could come from the side chains of FEMA in the (meth)acrylic network. Indeed, a sample was prepared without FEMA in their structure and the fraction of volatile components was significantly reduced. We suspect that there must be side reactions under elevated temperatures and acid catalysis that may lead to the loss of aromatic side groups from FEMA and irreversible network rearrangements leading to the formation of non-dynamic bridges between (meth)acrylic chains. These results suggest that the reprocessing capabilities of these materials could be improved by removing FEMA from the formulations, although this would lead to an increase in the viscosity of the 3D-printable formulations. Future work is under way in order to elucidate the reaction mechanism leading to irreversible changes in the network structure and analyze the impact on the reprocessing capabilities of these materials.

4. Conclusions

In this work, a dual-curing vitrimer system was developed and evaluated, with particular focus on its performance in 3D printing via vat photopolymerization (VPP). The formulations offered key processing advantages, including low viscosity, fast cure rates, and excellent printability. In the intermediate state, all formulations exhibited high flexibility and low stiffness, with tensile moduli ranging from 0.97 to 2.33 MPa, tensile strengths between 0.57 and 1.61 MPa, and strains at break from 63 to 91 %, enabling reliable fabrication of large parts with minimal internal stress.

Upon thermal treatment, the epoxy reaction proceeded to completion, producing a rigid and homogeneous network. Final mechanical properties improved dramatically, with tensile moduli reaching 2.5–3.6 GPa, tensile strengths around 66 MPa, and glass transition temperatures (Tg) rising from 72 to 82 °C, demonstrating the significant structural reinforcement achieved after full curing. Mechanical tests under torsion and direct shear confirmed uniform and consistent behavior, with maximum shear stresses up to 50 MPa, highlighting the material's potential for structural applications.

The comparative analysis of intermediate and final states clearly illustrates the orthogonality of the dual-curing system: the acrylate stage provides processable flexibility and minimal shrinkage, while the epoxy stage governs the final network homogeneity and mechanical performance. Thermal treatment studies revealed measurable changes in relaxation behavior and Tg evolution, suggesting partial loss of chain-side groups involved in the dynamic exchange. These effects may reduce recyclability and increase network rigidity over time,

emphasizing the importance of considering the thermal stability of mono- and bifunctional monomers in vitrimer design. Understanding how thermally sensitive side groups influence network evolution is essential for developing high-Tg, high-performance 3D-printed components that retain their dynamic properties after multiple processing or recycling cycles.

CRediT authorship contribution statement

A. Escribá-Flores: Writing – original draft, Visualization, Validation, Investigation, Formal analysis. **Szymon Gaca:** Methodology, Investigation. **X. Fernández-Francos:** Writing – review & editing, Supervision, Resources, Project administration, Methodology, Conceptualization. **Sandra Schlögl:** Writing – review & editing, Supervision, Resources, Methodology. **A. Fabregat-Sanjuan:** Writing – review & editing, Supervision, Resources, Project administration, Methodology, Conceptualization.

Declaration of competing interest

The authors confirm that there are no financial or personal relationships that could have influenced the research presented in this paper.

Acknowledgements

This work was funded by the Spanish Ministry of Science and Innovation (MCIN/AEI/10.13039/501100011033) through R&D projects PID2020-115102RB769 C21, PID2020-115102RB-C22 and PID2023-147128OB-C21, and also by Generalitat de Catalunya (2021-SGR-154). Armando Escribá acknowledges to the Martí Franqués fellowship program (2021PMF-BS-08). X. Fernández Francos acknowledges the Serra-Húnter programme (Generalitat de Catalunya). Part of the research work was performed within the #horizoneurope20212027 programme under the Marie Skłodowska-Curie Doctoral Networks (MSCA-DN) grant agreement No 101073432. Funding was provided by the European Union. Part of the research work was also carried out within the COMET-Module project"Repairtecture" (project-no.: 904927) at the Polymer Competence Center Leoben GmbH (PCCL, Austria) within the framework of the COMET-program of the Federal Ministry for Climate Action, Environment, Energy, Mobility, Innovation and Technology and the Federal Ministry of Labour and Economy. The PCCL is funded by the Austrian Government and the State Governments of Styria, Upper and Lower Austria.

Appendix A. Supplementary data

Supplementary data to this article can be found online at https://doi.org/10.1016/j.reactfunctpolym.2025.106494.

Data availability

Data supporting this study's findings are available from the corresponding author upon request.

References

[1] M. Pagac, J. Hajnys, Q.P. Ma, L. Jancar, J. Jansa, P. Stefek, J. Mesicek, A review of vat photopolymerization technology: materials, applications, challenges, and future trends of 3d printing, Polymers (Basel) 13 (2021) 1–20, https://doi.org/10.3390/polym13040598.

[2] F. Zhang, L. Zhu, Z. Li, S. Wang, J. Shi, W. Tang, N. Li, J. Yang, The recent development of vat photopolymerization: a review, Addit. Manuf. 48 (2021) 102423, https://doi.org/10.1016/j.addma.2021.102423.

[3] W. Yang, M. Zhang, S. Peng, R. Pan, Y. Liu, Introduction to Vat Polymerization 3D Printing Technologies, in: Vat Photopolymerization Additive Manufacturing, Elsevier, 2024, pp. 1–28, https://doi.org/10.1016/B978-0-443-15487-4.00010-8.

[4] M. Porcarello, C. Mendes-Felipe, S. Lanceros-Mendez, M. Sangermano, Design of acrylated epoxidized soybean oil biobased photo-curable formulations for 3D printing, Sustain. Mater. Technol. 40 (2024) e00927, https://doi.org/10.1016/j.susmat.2024.e00927.

[5] H. Goodarzi Hosseinabadi, D. Nieto, A. Yousefinejad, H. Fattel, L. Ionov, A.K. Miri, Ink material selection and optical design considerations in DLP 3D printing, Appl. Mater. Today 30 (2023) 101721, https://doi.org/10.1016/j.apmt.2022.101721.

[6] J. Borrello, P. Nasser, J.C. Iatridis, K.D. Costa, 3D printing a mechanically-tunable acrylate resin on a commercial DLP-SLA printer, Addit. Manuf. 23 (2018) 374–380, https://doi.org/10.1016/j.addma.2018.08.019.

[7] J.-F. Tang, K.-W. Lin, T.-H. Lin, W.-C. Lin, Pioneering techniques for achieving high-resolution, ultrasmooth surfaces via LCD 3D printing technology, Addit. Manuf. 103 (2025) 104764, https://doi.org/10.1016/j.addma.2025.104764.

[8] B.J. Lee, K. Hsiao, G. Lipkowitz, T. Samuelsen, L. Tate, J.M. DeSimone, Characterization of a 30 μm pixel size CLIP-based 3D printer and its enhancement through dynamic printing optimization, Addit. Manuf. 55 (2022) 102800, https://doi.org/10.1016/j.addma.2022.102800.

[9] E. Behroodi, H. Latifi, F. Najafi, A compact LED-based projection microstereolithography for producing 3D microstructures, Sci. Rep. 9 (2019) 19692, https://doi.org/10.1038/s41598-019-56044-3.

[10] F. Kröger, R. Eichelmann, G. Sauter, A. Pollien, P. Tegeder, L.H. Gade, E. Blasco, Two-photon laser printing of 3D multicolor emissive polymer microstructures, RSC Applied Polymers 2 (2024) 847–856, https://doi.org/10.1039/D4LP00141A.

[11] L. Zhou, J. Fu, Y. He, A review of 3D printing technologies for soft polymer materials, Adv. Funct. Mater. 30 (2020), https://doi.org/10.1002/adfm.202000187.

[12] L. Pezzana, R. Wolff, G. Melilli, N. Guigo, N. Sbirrazzuoli, J. Stampfl, R. Liska, M. Sangermano, Hot-lithography 3D printing of biobased epoxy resins, Polymer (Guildf) 254 (2022) 125097, https://doi.org/10.1016/j.polymer.2022.125097.

[13] C. Noè, M. Hakkarainen, M. Sangermano, Cationic UV-curing of Epoxidized biobased resins, Polymers (Basel) 13 (2020) 89, https://doi.org/10.3390/polym13010089.

[14] A. Vilanova-Pérez, S. De la Flor, X. Fernández-Francos, À. Serra, A. Roig, Biobased imine Vitrimers obtained by photo and thermal curing procedures—promising materials for 3D printing, ACS Appl Polym Mater (2023), https://doi.org/10.1021/acsapm.3c03234.

[15] S. Gaca, K. Dietliker, E. Rossegger, S. Schlögl, Design of photocurable thiol-epoxy resins for the processing of vitrimers with vat photopolymerisation 3D printing, React. Funct. Polym. 205 (2024) 106085, https://doi.org/10.1016/j.reactfunctpolym.2024.106085.

[16] A. Roig, X. Ramis, S. De la Flor, À. Serra, Dual-cured thermosets from glycydil methacrylate obtained by epoxy-amine reaction and methacrylate homopolymerization, React. Funct. Polym. 159 (2021) 1–11, https://doi.org/10.1016/j.reactfunctpolym.2021.104822.

[17] A. Roig, X. Ramis, S. De la Flor, À. Serra, Dual-cured thermosets based on eugenol derivatives and thiol chemistry, Eur. Polym. J. 200 (2023) 112499, https://doi.org/10.1016/j.eurpolymj.2023.112499.

[18] J. Casado, A. Faja, S. Moradi, X. Ramis, O. Konuray, X. Fernández-Francos, Reprocessable epoxy-acrylate 3D-printing resins with improved compatibility, React. Funct. Polym. 214 (2025) 106309, https://doi.org/10.1016/j.reactfunctpolym.2025.106309.

[19] K. Yu, P. Taynton, W. Zhang, M.L. Dunn, H.J. Qi, Influence of stoichiometry on the glass transition and bond exchange reactions in epoxy thermoset polymers, RSC Adv. 4 (2014) 48682–48690, https://doi.org/10.1039/C4RA06543C.

[20] J.P. Brutman, D.J. Fortman, G.X. De Hoe, W.R. Dichtel, M.A. Hillmyer, Mechanistic study of stress relaxation in urethane-containing polymer networks, J. Phys. Chem. B 123 (2019) 1432–1441, https://doi.org/10.1021/acs.jpcb.8b11489.

[21] R. Hajj, A. Duval, S. Dhers, L. Avérous, Network design to control Polyimine Vitrimer properties: physical versus chemical approach, Macromolecules 53 (2020) 3796–3805, https://doi.org/10.1021/acs.macromol.0c00453.

[22] A. Vilanova-Pérez, M. Surós, À. Serra, S. De la Flor, A. Roig, Custom-shaped malleable, recyclable and reversible structural adhesives based on vanillin polyimine vitrimers, React. Funct. Polym. 206 (2025) 106109, https://doi.org/10.1016/j.reactfunctpolym.2024.106109.

[23] U. Shaukat, A. Thalhamer, E. Rossegger, S. Schlögl, Dual-vat photopolymerization 3D printing of vitrimers, Addit. Manuf. 79 (2024) 103930, https://doi.org/10.1016/J.ADDMA.2023.103930.

[24] A. Vilanova-Pérez, S. Moradi, O. Konuray, X. Ramis, A. Roig, X. Fernández-Francos, Harnessing disulfide and transesterification bond exchange reactions for recyclable and reprocessable 3D-printed vitrimers, React. Funct. Polym. 195 (2024) 105825, https://doi.org/10.1016/J.REACTFUNCTPOLYM.2023.105825.

[25] S. Moradi, X. Fernández-Francos, O. Konuray, X. Ramis, Recyclable dual-curing thiol-isocyanate-epoxy vitrimers with sequential relaxation profiles, Eur. Polym. J. 196 (2023) 112290, https://doi.org/10.1016/J.EURPOLYMJ.2023.112290.

[26] A.M. Hubbard, Y. Ren, A. Sarvestani, D. Konkolewicz, C.R. Picu, A.K. Roy, V. Varshney, D. Nepal, Recyclability of Vitrimer materials: impact of catalyst and processing conditions, ACS Omega 7 (2022) 29125–29134, https://doi.org/10.1021/acsomega.2c02677.

[27] A. Romano, O. Konuray, F. Román, Y. Calventus, X. Fernández-Francos, I. Roppolo, M. Sangermano, Critical analysis of the thermal stability of transesterification vitrimers for <scp>3D</scp> −printing applications based on digital light processing, Polym. Int. 73 (2024) 280–286, https://doi.org/10.1002/pi.6592.

[28] J. Casado, A. Faja, S. Moradi, X. Ramis, O. Konuray, X. Fernández-Francos, Reprocessable epoxy-acrylate 3D-printing resins with improved compatibility, React. Funct. Polym. 214 (2025), https://doi.org/10.1016/j.reactfunctpolym.2025.106309.

[29] A.A. Escriba-Flores, X. Fernández-Francos, F. Ferrando, A. Fabregat-Sanjuan, Evaluation of the effect of coupling agent on the kinetic and mechanical properties of a 3D printable dual curing epoxy/acrylate system, Eur. Polym. J. 229 (2025) 113878, https://doi.org/10.1016/j.eurpolymj.2025.113878.
[30] A.A. Escriba-Flores, X. Fernández-Francos, F. Ferrando, A. Fabregat-Sanjuan, Tunable dual-curing acrylic/epoxy systems for 3D printing with enhanced joint performance via carbon nanotubes, Polymer (Guildf) 334 (2025) 128768, https://doi.org/10.1016/j.polymer.2025.128768.
[31] M. Fang, X. Liu, Y. Feng, B. Lu, M. Huang, C. Liu, C. Shen, Influence of Zn2+ catalyst stoichiometry on curing dynamics and stress relaxation of polyester-based epoxy vitrimer, Polymer (Guildf) 278 (2023) 126010, https://doi.org/10.1016/j.polymer.2023.126010.
[32] A. Al Rashid, W. Ahmed, M.Y. Khalid, M. Koç, Vat photopolymerization of polymers and polymer composites: processes and applications, Addit. Manuf. 47 (2021) 102279, https://doi.org/10.1016/j.addma.2021.102279.
[33] R. Geissberger, J. Maldonado, N. Bahamonde, A. Keller, C. Dransfeld, K. Masania, Rheological modelling of thermoset composite processing, Compos B Eng 124 (2017) 182–189, https://doi.org/10.1016/j.compositesb.2017.05.040.
[34] S.K. Romberg, A.P. Kotula, Simultaneous rheology and cure kinetics dictate thermal post-curing of thermoset composite resins for material extrusion, Addit. Manuf. 71 (2023) 103589, https://doi.org/10.1016/j.addma.2023.103589.
[35] J.-P. Pascault, H. Sautereau, J. Verdu, R.J.J. Williams, Thermosetting polymers, CRC Press, 2002, https://doi.org/10.1201/9780203908402.
[36] J. Smith-Jones, N. Ballinger, N. Sadaba, X. Lopez de Pariza, Y. Yao, S.L. Craig, H. Sardon, A. Nelson, 3D printed modular piezoionic sensors using dynamic covalent bonds, RSC Applied Polymers 2 (2024) 434–443, https://doi.org/10.1039/D3LP00289F.
[37] M. Bergoglio, G. Palazzo, D. Reisinger, M. Porcarello, G. Kortaberria, S. Schlögl, M. Sangermano, Cationic UV-curing of bio-based epoxidized castor oil vitrimers with electrically conductive properties, React. Funct. Polym. 200 (2024) 105936, https://doi.org/10.1016/j.reactfunctpolym.2024.105936.
[38] W. Huang, Z. Zu, Y. Huang, H. Xiang, X. Liu, UV-curing 3D printing of high-performance, recyclable, biobased photosensitive resin enabled by dual-crosslinking networks, Addit. Manuf. 91 (2024) 104352, https://doi.org/10.1016/j.addma.2024.104352.
[39] H. Gao, Y. Sun, M. Wang, Z. Wang, G. Han, L. Jin, P. Lin, Y. Xia, K. Zhang, Mechanically robust and Reprocessable acrylate Vitrimers with hydrogen-bond-integrated networks for photo-3D printing, ACS Appl. Mater. Interfaces 13 (2021) 1581–1591, https://doi.org/10.1021/acsami.0c19520.
[40] S. Grauzeliene, A.-S. Schuller, C. Delaite, J. Ostrauskaite, Development and digital light processing 3D printing of a Vitrimer composed of glycerol 1,3-Diglycerolate Diacrylate and Tetrahydrofurfuryl methacrylate, ACS Appl Polym Mater 5 (2023) 6958–6965, https://doi.org/10.1021/acsapm.3c01018.
[41] L. Ballester-Bayarri, A. Pascal, J. Ayestaran, A. Gonzalez, N. Ballard, R. Aguirresarobe, 3D printing of Vinylogous urethane-based Methacrylic covalent adaptable networks by vat Photopolymerization, ACS Appl Polym Mater 6 (2024) 2594–2603, https://doi.org/10.1021/acsapm.3c02777.
[42] X. Wu, X. Yang, R. Yu, X.-J. Zhao, Y. Zhang, W. Huang, A facile access to stiff epoxy vitrimers with excellent mechanical properties *via* siloxane equilibration, J. Mater. Chem. A Mater. 6 (2018) 10184–10188, https://doi.org/10.1039/C8TA02102C.
[43] D. Reisinger, A. Hellmayr, M. Paris, M. Haas, T. Griesser, S. Schlögl, Spatially resolved photoactivation of dynamic exchange reactions in 3D-printed thiol–ene vitrimers, Polym. Chem. 14 (2023) 3082–3090, https://doi.org/10.1039/D3PY00377A.
[44] H. Li, B. Zhang, R. Wang, X. Yang, X. He, H. Ye, J. Cheng, C. Yuan, Y. Zhang, Q. Ge, Solvent-free upcycling Vitrimers through digital light processing-based 3D printing and bond exchange reaction, Adv. Funct. Mater. 32 (2022), https://doi.org/10.1002/adfm.202111030.
[45] A. Liguori, E. Oliva, M. Sangermano, M. Hakkarainen, Digital Light Processing 3D Printing of Isosorbide- and Vanillin-Based Ester and Ester–Imine Thermosets: Structure–Property Recyclability Relationships, ACS Sustain. Chem. Eng. 11 (2023) 14601–14613, https://doi.org/10.1021/acssuschemeng.3c04362.
[46] S. Grauzeliene, A.-S. Schuller, C. Delaite, J. Ostrauskaite, Biobased vitrimer synthesized from 2-hydroxy-3-phenoxypropyl acrylate, tetrahydrofurfuryl methacrylate and acrylated epoxidized soybean oil for digital light processing 3D printing, Eur. Polym. J. 198 (2023) 112424, https://doi.org/10.1016/j.eurpolymj.2023.112424.
[47] J. Casado, O. Konuray, G. Benet, X. Fernández-Francos, J.M. Morancho, X. Ramis, Optimization and testing of hybrid 3D printing Vitrimer resins, Polymers (Basel) 14 (2022) 5102, https://doi.org/10.3390/polym14235102.
[48] A. Romano, O. Konuray, F. Román, Y. Calventus, X. Fernández-Francos, I. Roppolo, M. Sangermano, X. Fernández-Francos, I. Roppolo, M. Sangermano, Critical analysis of the thermal stability of transesterification vitrimers for 3D-printing applications based on digital light processing, Polym Int n/a (2023), https://doi.org/10.1002/pi.6592.